

RaLiBEV: Radar and LiDAR BEV Fusion Learning for Anchor Box Free Object Detection Systems

Yanlong Yang*, Jianan Liu*[†], Tao Huang[†], *Senior Member, IEEE*,
Qing-Long Han, *Fellow, IEEE*, Gang Ma, and Bing Zhu, *Member, IEEE*

Abstract—In autonomous driving, LiDAR and radar are crucial for environmental perception. LiDAR offers precise 3D spatial sensing information but struggles in adverse weather like fog. Conversely, radar signals can penetrate rain or mist due to their specific wavelength but are prone to noise disturbances. Recent state-of-the-art works reveal that the fusion of radar and LiDAR can lead to robust detection in adverse weather. The existing works adopt convolutional neural network architecture to extract features from each sensor data, then align and aggregate the two branch features to predict object detection results. However, these methods have low accuracy of predicted bounding boxes due to a simple design of label assignment and fusion strategies. In this paper, we propose a bird’s-eye view fusion learning-based anchor box-free object detection system, which fuses the feature derived from the radar range-azimuth heatmap and the LiDAR point cloud to estimate possible objects. Different label assignment strategies have been designed to facilitate the consistency between the classification of foreground or background anchor points and the corresponding bounding box regressions. Furthermore, the performance of the proposed object detector is further enhanced by employing a novel interactive transformer module. The superior performance of the methods proposed in this paper has been demonstrated using the recently published Oxford Radar RobotCar dataset. Our system’s average precision significantly outperforms the state-of-the-art method by 13.1% and 19.0% at Intersection of Union (IoU) of 0.8 under ‘Clear+Foggy’ training conditions for ‘Clear’ and ‘Foggy’ testing, respectively.

Index Terms—Autonomous driving, anchor box free object detection, LiDAR, point cloud, radar, range-azimuth heatmap, label assignment, bird eye’s view fusion, interactive transformer, deep learning.

I. INTRODUCTION

AUTONOMOUS driving systems typically employ sensors such as LiDAR, cameras, and radar to construct their perception functionality, which serves as the essential for the downstream tasks like trajectory prediction and ego motion planning [1, 2], etc. Such perception scheme has been

This work has been submitted to the IEEE for possible publication. Copyright may be transferred without notice, after which this version may no longer be accessible.

*Both authors contribute equally to the work and are co-first authors.

[†]Corresponding authors.

Y. Yang and G. Ma are with Vanjee Technology, Beijing, 100193, P.R. China. Email: {yangyanlong, magang}@wanji.net.cn.

J. Liu is with Vitalent Consulting, Gothenburg, 45197, Sweden. Email: jianan.liu@vitalent.se.

T. Huang is with the College of Science and Engineering, James Cook University, Cairns, QLD 4870, Australia. Email: tao.huang1@jcu.edu.au.

Q.-L. Han is with the School of Science, Computing and Engineering Technologies, Swinburne University of Technology, Melbourne, VIC 3122, Australia. Email: qhan@swin.edu.au.

B. Zhu is with the School of Automation Science and Electrical Engineering, Beihang University, Beijing, 100191, P.R. China. Email: zhubing@buaa.edu.cn.

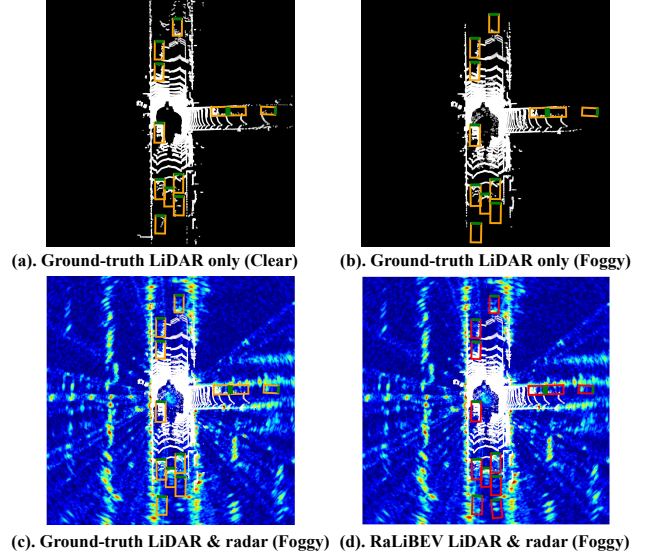


Fig. 1. Performance of the RaLiBEV in clear and foggy weather. The LiDAR and radar visualization results are combined by radar range azimuth heatmap with jet pseudo-color in the background and LiDAR with white point cloud and 2D object bounding boxes. The ground-truth boxes are orange, and the predicted boxes by RaLiBEV are red. All the boxes use green lines to indicate the heading direction.

widely demonstrated in numerous works, covering various aspects such as data collection/generation [3, 4], algorithm development [5], and real-world testing [6]. LiDAR, a key sensor used in Advanced Driver Assistance Systems (ADAS) and autonomous driving, offers rich semantic and geometric information for environmental perception tasks [7]. These tasks include object detection [8, 9], multi-object tracking [10, 11], ego localization [5, 12], and mapping [13]. Recent works show that fusing LiDAR and camera data at the raw stream level can significantly improve the robustness of autonomous driving perception systems [14, 15]. However, the performance of either camera or LiDAR can severely drop in adverse weather, i.e., rain, snow, and fog [16, 17]. For instance, cameras can become blurred, the operating range of LiDAR might be significantly reduced, and the number of noise points might increase due to the impact of heavy snow or fog. As illustrated in Fig. 1(b), the number of noisy points around the ego vehicle increases while the far end LiDAR points disappear, compared to the LiDAR point cloud measured in clear weather, as shown in Fig. 1(a).

In contrast with cameras and LiDAR, radar can naturally avoid the influence of adverse weather since the millimeter wavelength signals can penetrate the rain, snow, and fog. Such characteristic makes radar a powerful complementary sensor in

addition to either camera or LiDAR in ADAS and autonomous driving [18], and even in future cooperative perception [19]. The typical Frequency Modulated Continuous Wave (FMCW) radar, widely used in automotive systems, can accurately separate objects in range and speed dimension but has a low angular resolution due to the limited number of antennas in the compact space. Thus, radar can only provide many sparser detection points with ambiguity in angular information compared to the dense LiDAR point cloud. Such a drawback caused limitations on its performance when applied in the perception system [20–23].

To take full advantage of the robustness of radar in adverse weather, radar range-azimuth heatmap rather than detection points has been employed to fuse with LiDAR point cloud for vehicle detection in the recent proposed anchor box-based methods [24, 25]. However, their methods suffer from generalization issues since their approaches require predefined anchor boxes and they need to be carefully chosen according to the dataset. Moreover, these methods have been shown to have unsatisfactory performance, especially in the performance with high accuracy requirements.

To address these issues, we propose radar and LiDAR in Bird’s Eye View (BEV) fusion model, dubbed as RaLiBEV, for object detection. RaLiBEV introduces a novel object detection approach that fuses radar and LiDAR data in BEV in anchor boxes free scheme, intended for real-time application. The LiDAR point cloud is transformed into a structured data format in BEV, a process known as pillarization, while the radar range-azimuth heatmap naturally provides discrete sampling in BEV. These BEV feature maps from both radar and LiDAR are then separately extracted and combined to create an aggregated BEV feature map. This map is processed through the network’s backbone and then fed into a multi-scale detection head that doesn’t rely on anchor boxes to estimate the bounding boxes of vehicles.

Unlike the anchor box-based approach, the anchor box-free detection head first identifies representative pixels, or key points, in the predicted feature map. These key points are then used as positive samples to regress the remaining feature channels. However, this approach can lead to inconsistencies between the classification of foreground and background, and the regression problem. Specifically, a key point with a high classification score doesn’t necessarily result in better accuracy in bounding box regression. Another challenge lies in effectively fusing the rich feature information from the radar range-azimuth heatmap with the LiDAR feature map in a complementary manner, rather than simply concatenating them.

To address these issues, RaLiBEV incorporates innovative label assignment strategies to reduce the inconsistency between foreground-background classification and regression. Additionally, it employs interactive transformer-based BEV fusion techniques to better explore the interaction between radar and LiDAR feature maps. The experiment results demonstrate that our method outperforms the state-of-the-art method by 13.1% and 19.0% at IoU equals 0.8 in clear and foggy weather testing respectively.

The main contributions of this paper are concluded as

below:

- A radar and LiDAR BEV fusion-based anchor box free object detector, RaLiBEV, is proposed. The RaLiBEV can generate accurate 2D bounding boxes in BEV by fusion of features extracted from the radar range-azimuth heatmap and the LiDAR point cloud.
- A novel label assignment strategy, Gaussian Area-based Consistent Heatmap and IoU Cost Positive Sample Assignment (GACHIPS), is proposed to combat the inconsistency between the classification of key points and the corresponding bounding box regression tasks in the anchor box free object detector.
- A novel interactive transformer-based fusion module, Dense Query Map-based Interactive BEV Fusion (DQMITBF), is proposed to fuse radar and LiDAR feature maps. With the introduction of dense, learnable queries and a symmetric fusion architecture, the fusion module provides an information-sensitive fusion mechanism to aggregate suitable features from both maps under various weather conditions.
- The aforementioned object detector can achieve fairly accurate detection performance even in adverse weather, as shown in of Fig. 1(d) compared to the ground-truth bounding boxes illustrated in Fig. 1(c) which outperforms the state-of-the-art radar and LiDAR fusion-based object detector with a large margin in the popular Oxford Radar RobotCar (ORR) dataset [3].

The rest of this paper is organized as follows. Section II discusses the related works, including LiDAR-based perception methods, radar-based perception methods, and the methods which fuse radar and LiDAR for object detection. In Section III, the proposed radar and LiDAR fusion-based object detection approach, RaLiBEV, is introduced. In addition, the proposed label assignment strategies and interactive transformer-based fusion schemes are also described. Then, the experiment process and corresponding results on ORR datasets are explained and analyzed in Section IV. Finally, the conclusion and further work are drawn in Section V.

II. RELATED WORKS

A. LiDAR-based Object Detection

LiDAR is a widely used sensor in surrounding environment perception, and object detection is one of the most important missions in environment perception. The LiDAR object detection method based on deep learning can be divided into four categories according to the processing approach on the input point cloud.

The first approach is the point-based method. It implements a linear layer to extract features on unordered point cloud [26, 27]. The second approach is the grid-based method. This method discretizes the point cloud into 2D grids or 3D voxels, then applies CNN for further feature extraction [8, 9, 28, 29]. The third approach is the graph-based method, which transforms point cloud as graph data format [30]. The Graph Neural Network (GNN) is employed for extracting the feature and detecting the objects, where the points are defined as vertices and the relations between points are defined as edges. The

fourth type is the combination method. One way is to combine features extracted from two different representations of the point cloud, such as points features and grid/voxel features [31]. Another way is to concatenate features from different views of 2D grids, such as range view and BEV, and decode concatenated features by 2D CNN afterward [32]. Although LiDAR can provide precise and dense 3D spatial information, the inherent problem of facing adverse weather still limits its performance.

B. Radar-based Object Detection

Radar, utilizing under-millimeter wave band electromagnetic signals, is capable of penetrating adverse weather conditions, making it effective for object detection under noise. Both conventional and deep learning methods are employed for this task.

Conventional methods, such as Constant False Alarm Rate (CFAR) algorithms [33] and clustering techniques [34], dynamically adjust the detection threshold based on noise levels and group detected points into objects. However, these methods may struggle with complex environments and overlapping objects. Deep learning methodologies initiate the processing of radar point clouds, employ semantic segmentation for categorization and utilize clustering techniques for the assembly of objects [35, 36]. This method provides detailed object detection but requires significant computational resources. More recent approaches, such as PointNet models [37, 38] and Graph Neural Networks (GNNs) [39, 40], process point cloud data directly. PointNet learns complex patterns for object detection and classification, while GNNs capture both local and global patterns for enhanced detection accuracy. These methods build a end-to-end points-based object detection pipeline for radar object detection. However both methods require substantial training data and computational resources. Lastly, range-azimuth heatmaps are used for radar object detection. One approach applies clustering and classification to the heatmap [41, 42], while another uses deep learning models to directly predict object presence and location from the heatmap [43–47]. Methods leveraging heatmap-based techniques possess the capability to extract the most comprehensive information, albeit at the cost of increased computational resources.

Despite its ability to penetrate adverse weather, radar’s limitations, such as susceptibility to multi-path propagation and lower resolution, hinder detailed object recognition. These drawbacks underscore the necessity of sensor fusion in autonomous driving systems. The fusion of radar and LiDAR data, leveraging LiDAR’s high-resolution point cloud data, can significantly enhance object detection and recognition capabilities.

C. Radar and LiDAR Fusion-based Object Detection

Radar and LiDAR both have their strength and weaknesses. Fusing the information from the two types of sensors can achieve a better surrounding perception [24, 25, 48]. Generally, sensor fusion can be performed at the result or feature levels.

In result-level fusion, each sensor is characterized as an individual detection union. Then the detected objects are

collected to generate the final result. This method consumes less transmission bandwidth and has a fast operation speed. However, its performance is severely limited by each single sensor detector.

In feature-level fusion, it is essential to aggregate feature information from both sensors, providing rich and reliable data for end-to-end networks [49, 50]. General fusion strategies, such as concatenating or adding data from different sensors after CNN-based feature extraction, offer faster computational speeds but limited capacity in terms of weighted combination of feature information. Utilizing the attention mechanism proposed in transformers for information scraping has been demonstrated to be more effective [51]. However, previous works utilizing cross-attention, whether on different data channels or across different temporal data [24, 25, 52], suffer from certain effectiveness issues. This is because relying solely on attention to capture information without query limits the model’s flexibility to fit difficult samples. Bi-LRFusion [53] proposes a bidirectional LiDAR and radar feature fusion scheme, which uses a query-based approach guided by both elevation-view and bird’s-eye-view perspectives for fusing LiDAR and radar features. However, its utilization of sparse queries severely restricts its performance when handling dense radar range-azimuth heatmap data. To tackle this problem, we propose a dense, learnable query map-based transformer block that merges features from each sensor. This approach offers dense and adaptable attention weights for enhanced sensor fusion.

D. Label Assignment in Object Detection

The traditional label assignment design was initially proposed in anchor-based and anchor-free object detection frameworks. In these frameworks, fixed thresholds were used to determine whether a box or point is a positive sample, based on intuitive costs such as the IoU between anchor boxes and ground-truth boxes or whether an anchor point is inside a gt box. However, the biggest problem with these heuristic designs is that they ignore the issue of consistency between foreground-background classification and box regression [54], meaning that high-scoring anchor boxes or points may not always lead to the best box regression results. This gap can cause the model to select suboptimal boxes as output during inference, which lowers the model’s detection performance.

In anchor-based frameworks [55, 56], since all anchor boxes with an IoU greater than a certain threshold with the gt box need to calculate loss and regression, the loss is designed as a sum of foreground-background classification and box regression losses. The parallel loss design makes the two part independent of each other, leading to the aforementioned consistency problem. Similarly, in anchor-free frameworks [57–59], the fixed threshold label assignment uses some fixed anchor points inside the gt box as positive samples, such as center points or corner points. After calculating foreground-background classification loss and box regression loss separately and adding them together, there is still a numerical gap in regression. Again, the inconsistency problem prevails.

To address this problem, some works have attempted to focus on matching the predicted results and ground-truth by

combining label assignment with model prediction, such as freeAnchor [60], ATSS [61], AutoAssign [62], PAA [63] and OTA [64]. These methods evolved the solution for assigning positive and negative samples from matching anchors and gt boxes to aligning predicted outcomes with ground-truth. This approach maximally reduces the consistency gap for bounding box decoding mentioned earlier.

However, these methods primarily concentrate on image-based object detection, addressing challenges such as varying object sizes, aspect ratios, and mutual occlusion by assigning multiple positive samples to individual gt targets. Nevertheless, incorporating multiple positive samples inevitably results in competition among them during the training process, as they all contribute to the gradient. This exacerbates the consistency gap during the inference phase.

III. PROPOSED METHOD

In this section, the framework of the proposed anchor box-free radar and LiDAR fusion-based object detector are first introduced. Then, two enhancements of RaLiBEV, one with label-assignment strategies and the other with interactive transformer fusion strategies, are described.

A. Anchor Box Free Object Detection

Following the idea of sensor fusion, aggregating features from each sensor under BEV representation is straightforward. As depicted in Fig. 2, the raw LiDAR point cloud and radar range azimuth heatmap undergo pre-processing via their respective sensor branch’s feature extractors. These two features are then fed into fusion module for feature fusion. The combined features are subsequently processed by a YOLOV4-based [65] feature extractor and a multi-scale anchor-free object detection head to decode the 2D BEV rotating bounding boxes detection result.

Specifically, the radar data is converted from polar to Cartesian coordinates by applying bilinear interpolation, so the final structure shape of the data shows as $[W_r, H_r, C_r]$. The W, H, C denote width, height and channel of the feature map respectively. For LiDAR data, since the point cloud is an unordered 3D points set, the data needs to be structured before subsequent operations. Therefore the method of PointPillars [9] is applied to form the input LiDAR data into a fixed shape $[W_l, H_l, C_l]$ under BEV.

After the pre-processing, N convolution layers on each branch are applied to extract features without downsampling. Then two branch data are fused with an interactive transformer module and sent into the YOLOv4 backbone for further feature extraction.

A multi-scale anchor-free detection head is added at the end to decode the detection results. The first output channel of the detection head is a predicted heatmap, representing the object’s existence probability. The second to the last channel represent $\Delta x, \Delta y$, width, length, angle classification, angle offset, and object class, respectively. Δx and Δy denote the predicted box center offset in x and y direction. Two channels are set to help angle regression. One is an angle classification channel, the other is an angle offset regression channel.

Following the state-of-the-art anchor-free detection paradigm, the positive anchor points of the feature map should be specified first, then start regression based on those locations. For each ground-truth bounding box in the BEV, a Gaussian distribution map is generated under each head scale. This serves as a supervision signal to train the network for heatmap prediction in a supervised learning approach. The generation method can be described by:

$$G(\mathbf{x}|\boldsymbol{\mu}, \boldsymbol{\Sigma}) = \frac{1}{2\pi^{\frac{d}{2}} |\boldsymbol{\Sigma}|^{\frac{1}{2}}} e^{-\frac{1}{2}(\mathbf{x}-\boldsymbol{\mu})^T \boldsymbol{\Sigma}^{-1}(\mathbf{x}-\boldsymbol{\mu})}, \quad (1)$$

where the $\mathbf{x} = [i, j]$ is the BEV spatial vector, and i, j range from 0 to number of grid on the feature map. d is the dimension of \mathbf{x} . $\boldsymbol{\mu}$ is the mean of \mathbf{x} , which is the center coordinates of ground-truth boxes. $\boldsymbol{\Sigma}$ is a covariance matrix of the distribution, which can be calculated by:

$$\boldsymbol{\Sigma} = E(\mathbf{x} - E(\mathbf{x}))(\mathbf{x} - E(\mathbf{x}))^T, \quad (2)$$

where the four corners’ 2D coordinates of a box are used as \mathbf{x} , and the $E(\mathbf{x})$ equals the center coordinates of the box. Such operation is done iteratively over all ground-truth objects in one time frame, thus a ground-truth Gaussian mixture distribution is generated.

B. Label Assignment Strategies

For an object detection problem, the total loss, in general, can be described as the sum of foreground-background classification loss and box regression loss, as shown here:

$$\mathcal{L} = \mathcal{L}_{cls} + \mathcal{L}_{box}, \quad (3)$$

where the \mathcal{L}_{cls} is the foreground-background classification loss implemented with focal loss [66], the \mathcal{L}_{box} is the box regression loss implemented with smooth L1 loss. The focal loss is modified with Gaussian mixture distribution weight $G_{i,j}$:

$$\mathcal{L}_{cls} = \begin{cases} - \sum_{i,j=0}^M G_{i,j} (1 - p_{i,j})^\gamma \log(p_{i,j}) & \text{if } G_{i,j} = 1, \\ - \sum_{i,j=0}^M G_{i,j} p_{i,j}^\gamma \log(1 - p_{i,j}) & \text{otherwise.} \end{cases} \quad (4)$$

M is the grid number of feature map. $G_{i,j} \in [0, 1]$ specifies each element in the ground-truth Gaussian mixture distribution generated from Eq. (1). $p_{i,j} \in [0, 1]$ is the model’s estimated value for each anchor point on BEV feature map, and γ is a static parameter that balances the weight of positive and negative samples. By weighting the gradient with a Gaussian weight, the model’s convergence will be more stable and quicker [58].

The box loss is consist of $\Delta x, \Delta y$, width, length and angle offset $\Delta\theta$ loss, which are in the formulation of smooth L1 loss. While for the angle classification loss, the cross-entropy loss l_θ^{ce} is applied:

$$\mathcal{L}_{box} = \sum_{i,j=0}^M \alpha_{i,j} (l_{\Delta xy}^{reg} + l_{wl}^{reg} + l_\theta^{ce} + l_{\Delta\theta}^{reg}). \quad (5)$$

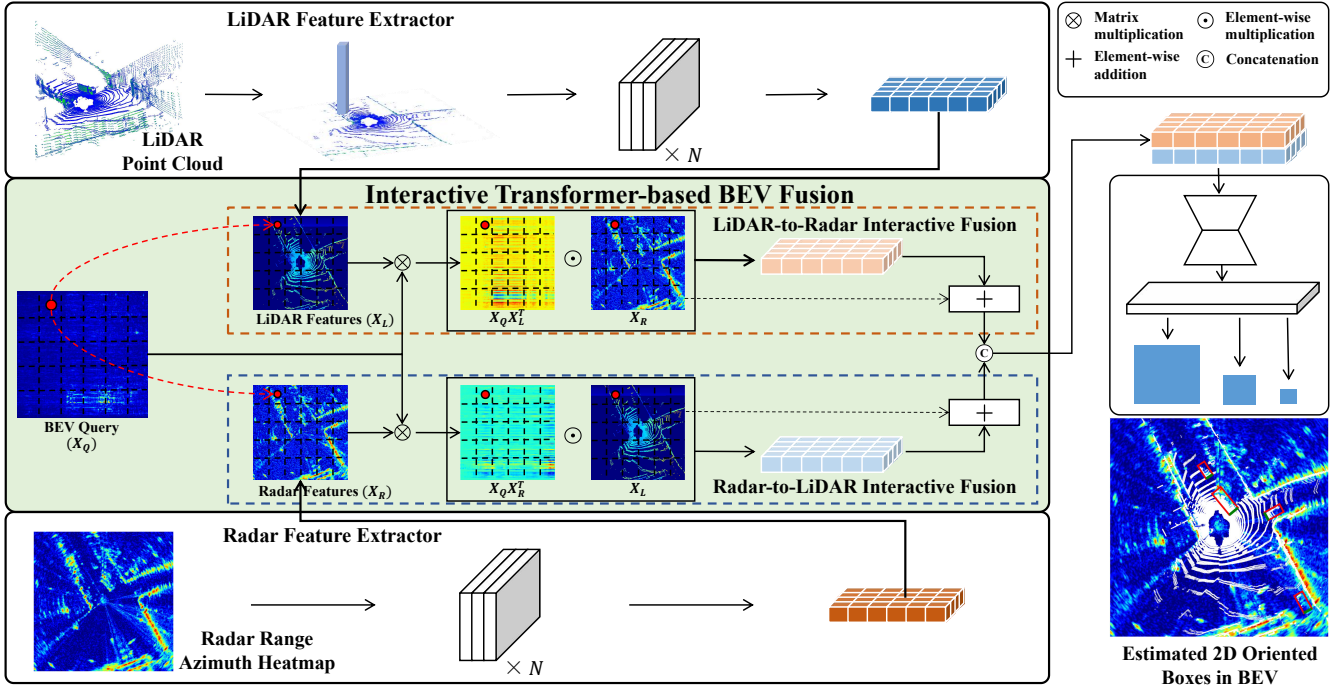


Fig. 2. The entire pipeline of proposed radar and LiDAR fusion-based anchor box free object detector, RaLiBEV.

where $\alpha_{i,j} \in \{0, 1\}$ is the binary element of mask matrix α . Typically, α is utilized to control which anchor points on the BEV feature map are selected for calculating the box loss. The chosen samples are referred as positive samples, denoting by $\alpha_{i,j} = 1$, while the unselected ones are termed as negative samples with $\alpha_{i,j} = 0$.

The box regression loss could only occur on the positive samples, while the foreground-background classification loss is computed upon every anchor point on the feature map. This leads to the problem that an anchor point with a higher foreground-background classification score does not always index the best bounding box regression result during decoding the predicted object. This is known as the inconsistency problem in label assignments. A label assignment strategy with lesser inconsistency between foreground-background classification and box regression can decrease the model’s miss-detection rate and help achieve higher detection accuracy.

Typically, three strategies of label assignment could be applied, including bipartite matching, multi-positive label assignment, and single-positive label assignment. “Multi/single” indicates how many anchor points can be chosen as the positive sample for one object.

1) *Bipartite Matching Label Assignment*: The typical bipartite matching label assignment is based on the Hungarian algorithm. This set-based label assignment builds a cost matrix of IoU between predicted and ground-truth boxes, where the predicted boxes are decoded from a predefined location. Then it finds the best matching positive samples by the Hungarian algorithm. The traditional bipartite matching process is based on anchors [67], while DETR [68] leveraging object query changes this matching art to a total end-to-end style. Using the Hungarian algorithm, DETR computes loss directly between predefined object queries and ground-truth object boxes. Then

after training, the converged queries can be directly decoded into the final predicted boxes without Non-Maximum Suppression (NMS). However, the size of the query map in our proposed method is set to be the same as the size of the radar and LiDAR feature map. Such a large number of queries leads to massive computational consumption, which is not feasible when applying the Hungarian algorithm. Thus, such bipartite matching label assignment is not considered for our proposed method.

2) *Multi-Positives Label Assignment*: Following the idea that multiple positive anchor points may alleviate positive and negative sample imbalance problems in anchor-free detection architecture, a Gaussian area-based multi-positive label assignment is designed. Based on the ground-truth Gaussian mixture distribution heatmap \mathbf{G} created in Section III-A, a static threshold is used to extract the specific region as the positive anchor points. Foreground-background classification and box regression are then applied together on each positive anchors points. As Fig. 3(b) shows, all dots with red colors are the selected positive samples. They are all located in the ground-truth Gaussian distribution yellow-colored area, thus this approach is named as *Gaussian Area-based Multi-Positives Sample assignment*.

Nonetheless, the introduction of multiple positive samples inevitably leads to competition in training procedure among them because they all devote to the gratitude, exacerbating the consistency gap during the interference phase. The experiment result is shown later in Section IV-C1.

3) *Single Positive Label Assignment*: In order to prevent numerical regression conflicts caused by multiple positive samples, single positive sample allocation strategy has been designed. The fundamental characteristic of a single positive sample is that, for each ground-truth object, there is only one

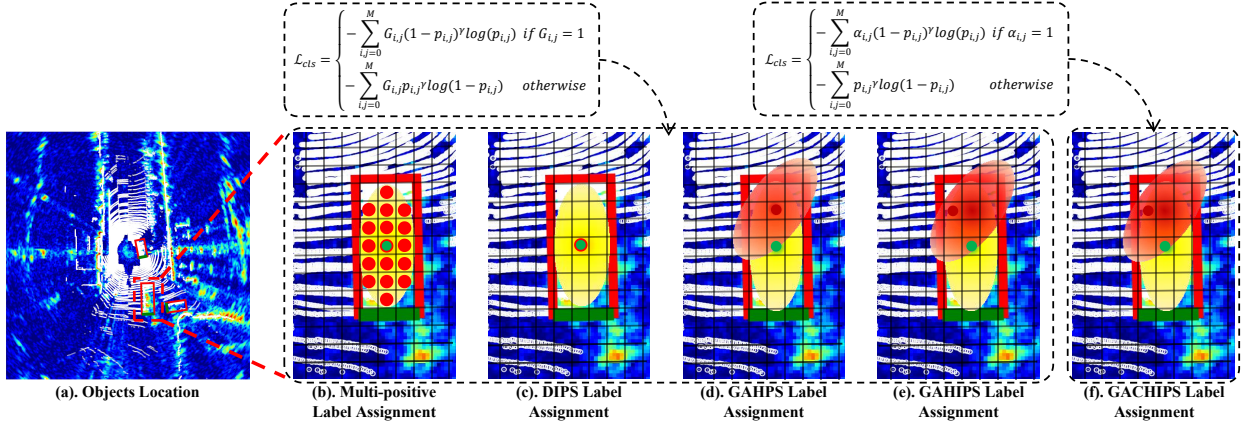


Fig. 3. Overview of label assignment strategies for object detection. (a) Identifies the object with a red-bordered ground-truth bounding box and a green headline. Yellow and red ellipses represent ground-truth and predicted Gaussian distributions, respectively. Red dots are positive sample points, and green dots mark the ground-truth Gaussian centers. Strategies (b) to (e) show different methods for selecting positive samples for box loss calculation, ranging from (b) using all anchor points within the ground-truth area, to (c) selecting the center. (d) the point with the highest foreground-background classification score, and (e) the point with the highest "score plus IoU". Strategy (f) integrates the approach from (e) with an alternative loss function as Eq. (14).

positive anchor point corresponding to it, which contributes to the gradient of the loss in each training iteration. Four methods have been proposed successively to alleviate the inconsistency between foreground-background classification and box regression mentioned in the previous discussion. The experiment shows that abandoning the center prior can most effectively alleviate the consistency issue between object detection and regression. The proposed four methods share the same training framework as below:

- ① Generate candidate anchor points: For each ground-truth object, create a set of candidate anchor points.
- ② Design unique costs: Assign a unique cost to each candidate anchor point.
- ③ Select positive samples: Choose the most suitable candidate anchor points as positive samples.
- ④ Compute loss: Calculate the loss result based on the selected positive anchor points.

The four label assignment strategies contribute different innovations in the pipeline. The details are elaborated below:

The first step is generating candidate anchor points. This step is the common procedure for all four label assignment strategies. According to Eq. (1), a Gaussian distribution $\{\mathbf{G}_k, k = 1, \dots, n\}$ is generated for each ground-truth object, and the multiple objects form a Gaussian mixture distribution \mathbf{G} . By setting a fixed threshold, the anchor points inside each Gaussian distribution can be obtained, which are called candidate anchor points. This steps can be described as:

$$\mathbf{A}_k^{\mathbf{G}} = \mathcal{A} \cap \mathbf{G}_k, \quad (6)$$

where $\mathbf{A}_k^{\mathbf{G}}$ represents the set of candidate anchor points in the k -th ground-truth Gaussian distribution, \mathcal{A} represents the set of all anchor points on the BEV grid, and \cap represents the intersection operation.

The second and third steps are to design unique cost for these candidate anchor points and then select one as positive sample. In this two steps, the first three label assignment strategies make improvements rely on different design:

- The first design is *Direct Index based Positive Sample (DIPS) assignment*. As Fig. 3(c) shows, DIPS treats the label center locations as the positive anchor points, then applies foreground-background classification and box regression on these anchor points. The DIPS sample assignment is a standard design of CenterPoint [8] whose cost and selection are described as:

$$a_k = \text{computeCenter}(\mathbf{A}_k^{\mathbf{G}}). \quad (7)$$

The process begins by determining if a candidate anchor point is positioned at the center of $\mathbf{A}_k^{\mathbf{G}}$. This is calculated and represented as a_k according to Eq. (7). Following this, a binary mask, symbolized as α , is used to indicate the selection of positive samples. This mask is assigned a value of 1 in accordance with:

$$\alpha(a_k) = 1. \quad (8)$$

After the establishment of α , the location for the box regression loss is pinpointed. Subsequently, the final loss is then calculated based on Eq. (3), which is summation of two values obtained from Eq. (4) and Eq. (5) for all the positive samples.

- The second approach is termed as the *Gaussian Area-based Heatmap cost Positive Sample (GAHPS) assignment*. In this method, we substitute the cost calculation from determining the centers of ground-truth boxes to assessing the maximum predicted heatmap value for each anchor point. The remaining steps, including the first and the fourth, are kept unchanged. Firstly, the model inferences predicted heatmap \mathbf{P}_k^{cls} and boxes \mathbf{P}_k^{box} follows Eq. (9). As illustrated in Fig. 3(d), the red fading ellipse represents the predicted Gaussian distribution heatmap. This step is described as:

$$\mathbf{P}_k^{cls}, \mathbf{P}_k^{box} = \text{Decode}(\mathbf{F}, \mathbf{A}_k^{\mathbf{G}}). \quad (9)$$

The decoding function, denoted as $\text{Decode}(\cdot)$, takes two inputs: the feature map \mathbf{F} and the anchor points in k -th

Gaussian distribution A_k^G . Then, different from DIPS, the cost is designed as predicted heatmap as shown in:

$$C_k^a = P_k^{cls}. \quad (10)$$

The anchor point with highest predicted heatmap value are chosen as the positive sample a_k as shown in:

$$a_k = \operatorname{argmax}(C_k^a). \quad (11)$$

The Eqs. (9), (10), and (11) are utilized to substitute Eq. (7). Following this, the binary mask α is computed using Eq. (8). Similar to the first DIPS strategy, the final loss is also calculated using Eq. (3), (4) and (5). However, the final loss is determined based on the established α here in this design.

- The third approach is termed as the *Gaussian Area-based Heatmap and IoU cost Positive Sample (GAHIPS) assignment*, as shown in Fig. 3(e). In this method, we go beyond merely substituting the cost with the predicted heatmap value. Instead, we replace it with the sum of the predicted heatmap value and the IoU value between the predicted box and the ground-truth box. Therefore, the first step is to calculate the IoU score of predicted bounding box and ground-truth box. The decoded P_k^{box} derived from Eq. (9) is utilized to compute the IoU scores S_k^{IoU} in relation to the ground-truth bounding boxes \mathcal{G}_k^{box} :

$$S_k^{IoU} = \operatorname{computeIoU}(P_k^{box}, \mathcal{G}_k^{box}). \quad (12)$$

Following this, the sum of the predicted heatmap values and IoU scores, represented as C_k^a , is employed as the new cost, as indicated in:

$$C_k^a = P_k^{cls} + S_k^{IoU}. \quad (13)$$

The positive anchor point a_k is then selected using Eq. (11), and the binary mask α is also determined by Eq. (8). Lastly, same as aforementioned strategies, the final loss is still calculated using Eq. (3), which is a combination of Eq. (5) and Eq. (4).

To be noted that, although the processes of determining α are different in DIPS, GAHPS and GAHIPS, the ways of computing final loss are same. However, because the foreground-background classification loss and box regression loss are independent from each other, such definition of final loss leads to a consistency gap between the two loss above. To address this issue, the fourth design is proposed.

- The fourth design is *Gaussian Area-based Consistent Heatmap and IoU cost Positive Sample (GACHIPS) assignment*, which is a divergence of the GAHIPS. GACHIPS follows the previous three steps as the GAHIPS, but modifies the final step of loss computation as indicated in Fig. 3(f). By doing it, the foreground-background classification loss and box regression loss are both controlled by α . Specifically, the former foreground-background classification loss function which is shown in Eq. (4), should be replaced by:

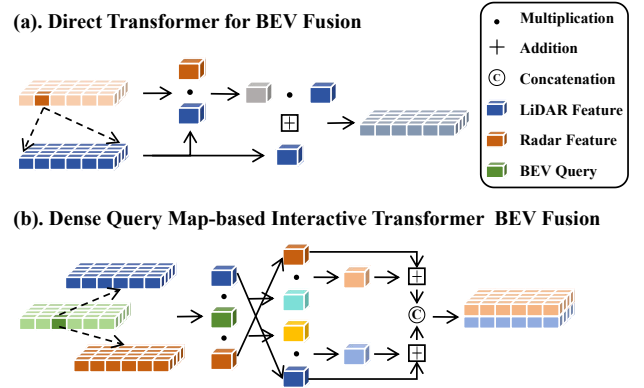


Fig. 4. Comparison of direct transformer for BEV fusion with dense query map-based interactive transformer for BEV fusion.

$$\mathcal{L}_{cls} = \begin{cases} - \sum_{i,j=0}^M \alpha_{i,j} (1 - p_{i,j})^\gamma \log(p_{i,j}) & \text{if } \alpha_{i,j} = 1, \\ - \sum_{i,j=0}^M p_{i,j}^\gamma \log(1 - p_{i,j}) & \text{otherwise.} \end{cases} \quad (14)$$

During inference procedure, the key step is to extract peaks from the predicted heatmap. We set a static threshold to pick every anchor point to generate the corresponding box, then NMS is applied to discard other boxes that overlap with the higher confidence box by a certain size. Beware that NMS can still filter out a certain amount of overlapping bounding boxes estimated from three branches in multiple scales. However, the estimated bounding boxes rarely overlap in a single scale branch since the anchor box-free approach with a single positive label assignment strategy is employed.

C. Interactive Transformer for Fusion of Radar and LiDAR in BEV

In the pursuit of enhancing the performance of sensor fusion in autonomous driving systems, we propose a novel approach that transcends the conventional method of simply concatenating features from each sensor. The standard transformer [51] based traditional approach, while straightforward, is inherently limited in its ability to effectively weigh the features from each sensor. To this end, we have designed an innovative interactive transformer-based BEV Fusion block, to fuse data from the two sensor branches more effectively.

The first approach *Direct Transformer for BEV Fusion*, depicted in Fig. 4(a), employs a plain transformer BEV fusion as a basic method. This method utilizes radar branch feature map as the query and LiDAR feature map as the key and value. The weight matrix is computed through matrix multiplication of the query and key, which is subsequently normalized using a softmax function. Then the dot product of the weight and value are added with value itself acting as a residual process. This process can be mathematically represented as follows:

$$\mathbf{X}_{out} = \sigma(\mathbf{X}_R \mathbf{X}_L^T) \odot \mathbf{X}_L + \mathbf{X}_L. \quad (15)$$

$$\mathbf{X}_{out} = (\sigma(\mathbf{X}_Q \mathbf{X}_R^T) \odot \mathbf{X}_L + \mathbf{X}_L) \textcircled{\circ} (\sigma(\mathbf{X}_Q \mathbf{X}_L^T) \odot \mathbf{X}_R + \mathbf{X}_R). \quad (16)$$

In this equation, \mathbf{X} represents the feature map, $\sigma(\cdot)$ denotes the softmax function, \odot denotes element-wise multiplication, and $\mathbf{X}_R, \mathbf{X}_L$ are radar and LiDAR feature maps. This method serves as a baseline to demonstrate the effectiveness of our second approach.

The second approach, shown in Fig. 4(b), named *Dense Query Map-based Interactive Transformer for BEV Fusion (DQMITBF)*, shares the core concept with the first approach but introduces a variation in the query definition. In this method, we define a randomly initialized learnable BEV query that shares the same size as the input key feature map. Interactive attention is computed between this learnable BEV query and both the radar and LiDAR feature maps, which are treated as the key and value, respectively. The interactive fusion of LiDAR and radar features through a BEV query involves a three-step process. Firstly, to facilitate radar-to-LiDAR interaction fusion, the BEV query is used to calculate the correlation between itself and the radar feature map. Secondly, the resulting softmax output is then utilized as a weighting factor for the LiDAR feature map. Finally, the weighted LiDAR feature map is added to the LiDAR feature itself. Similarly, the same fusion procedure is repeated for LiDAR-to-radar features. In the end, the fused radar and LiDAR feature maps are concatenated for further processing. The fusion process can be succinctly represented as Eq. (16). In this equation, \mathbf{X}_Q is the randomly initialized learnable query, \mathbf{X}_R and \mathbf{X}_L are the feature maps of radar and LiDAR, respectively. $\textcircled{\circ}$ is concatenation process.

The DQMITBF architecture interacts symmetrically with radar and LiDAR features through a BEV query and integrates them in a unified phase. This interactive query allows the model to prioritize feature-rich branches, especially in varying weather conditions. Thus, this novel approach optimizes the weighting and combination of heterogeneous sensor features in an adaptive manner, enhancing the effectiveness of autonomous driving systems in different meteorological scenarios.

IV. IMPLEMENTATION AND RESULTS

A. Dataset and Evaluation Metrics

The ORR dataset [3] is selected because it provides a synchronized LiDAR point cloud, radar range azimuth heatmap, car motion pose parameters, etc. The LiDAR point cloud was captured by two Velodyne HDL-32E LiDARs, each designed to cover one side of the car. On the top of the car locates a NavTech CTS350-X radar, which has a 360° field of view in the fashion of a mechanical scan. The angle resolution of radar data is 0.9° every 400ms, while LiDAR data angle resolution is 0.33° every 20ms.

The synchronization issue between LiDAR data and radar data and the annotation generation was solved by interpolation with the help of ego vehicle pose [24]. Specifically, the pose parameters compensated for the misalignment between the

LiDAR point cloud and radar range-azimuth heatmap. Utilizing the timestamps as a reference, [24] computes the motion between LiDAR point cloud and radar heatmap, then transfer every point to radar coordinate. The annotation bounding boxes are also created by [24] every 20 frames. The remaining frames' annotations were also generated by interpolation. For testing in a foggy scenario, MVDNet relocates the LiDAR point cloud with the method of DEF [48]. According to the fog model in DEF, MVDNet sets the fog probability to 0.05 to recompute a maximum visible range for every point. If the current point range is greater than the maximum foggy range, this point would be set rather lost or relocated as a scatter point. Following the same operations on data in MVDNet, the 2D label bounding boxes are used as supervision. Corresponding radar and LiDAR data in 8862 number frames are split into 7071 for training and 1791 for testing.

To evaluate the prediction result of the model, the 2D rotated bounding box average precision (AP) under different IoU thresholds is employed as a final evaluation metric. This metric simultaneously evaluates the precision and recall performance of the model under the test dataset. A higher AP value represents better prediction precision of the bounding box and a smaller missing detection rate of the objects. Prediction boxes can be defined as True Positive (TP) objects, which overlap with the ground-truth objects over the IoU threshold, or False Positive (FP) objects which overlap with ground-truth objects lesser than the IoU threshold. By setting different IoU thresholds, the number of TP and FP objects varies. Under a certain IoU threshold value, all the prediction boxes can be arranged as a TP/FP list sorted by their class scores. The precision and recall performance is defined as:

$$\begin{aligned} Precision &= \frac{TP}{TP + FP}, \\ Recall &= \frac{TP}{TP + FN}. \end{aligned} \quad (17)$$

The $TP + FP$ equals the total number of prediction objects, and the FP is the number of false prediction objects. While the FN is the number of miss-detection objects, $TP + FN$ equals the number of ground-truth objects.

The Table I shows an example of how the AP is calculated by setting the IoU threshold as 0.5. Assuming no miss-detected objects exist, all these predicted objects represented in the column are sorted by their scores. Precision and recall are computed according to Eq. (17) in each column. It is worth mentioning that the precision result drops and the recall increase, along with the decrease of the object's scores. The $AP@IoU=0.5$ is then defined as the area value enclosed under the precision-recall curve accordingly to reflect the trend of the precision-recall curve as a performance metric. The greater the AP value is, the better model performs.

B. Implementing Details

The preprocess of LiDAR data is based on PointPillars [9], where we set $0.2m \times 0.2m$ as our BEV spatial resolution. It

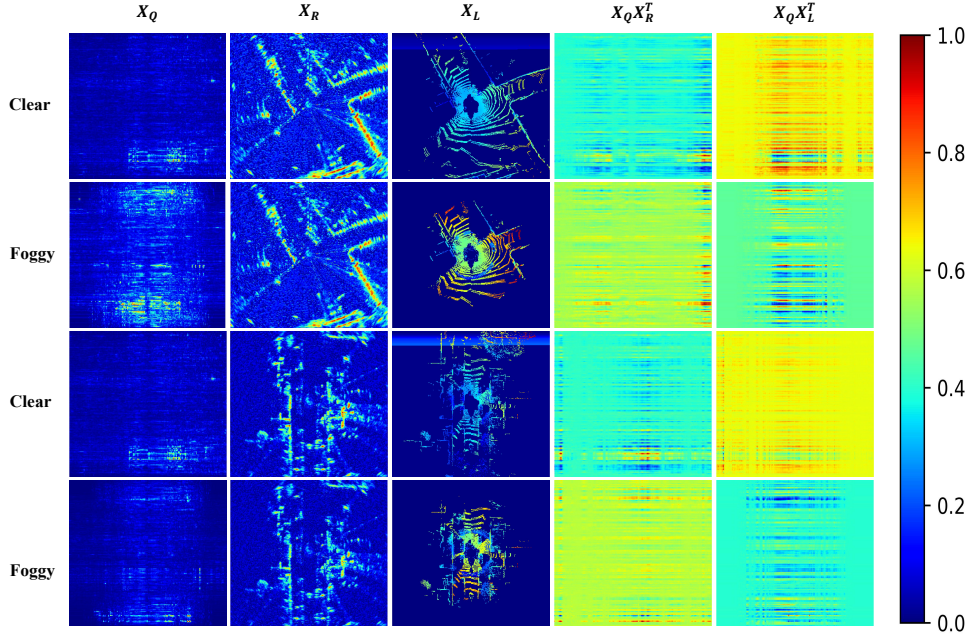


Fig. 5. Interactive transformer feature map visualization results.

TABLE I
EXAMPLE LIST OF PR CURVE AT IOU=0.5

Scores	0.98	0.97	0.96	0.95	0.94	0.92	0.91
Prediction Objects	TP	TP	FP	TP	TP	TP	FP
Precision	1	1	2/3	3/4	4/5	5/6	5/7
Recall	1/5	2/5	2/5	3/5	4/5	1	1

transforms the disordered LiDAR point cloud to a $320 \times 320 \times 9$ structured matrix. Meanwhile, the input radar data is in the format of $320 \times 320 \times 1$ under BEV, naturally. As Fig. 2 shows, the subsequent convolution block consists of a 3×3 convolution layer, a batch norm layer, and a leaky ReLU layer. The replication N of it is set as 3. The inference procedure decodes the predicted boxes from three scale output anchor-free heads. The static threshold is set to 0.1 to extract peaks (as key points among all anchor points) from the predicted heatmap. After generating boxes from three scale output feature maps, the NMS method is applied for deleting extra boxes, whose threshold is set as 0.2.

When training, the batch size is set to 32, and 4 Nvidia Tesla V100S GPUs are used. The first two epochs are used as a warming up. The learning rate linearly increases from 0 to 0.01 after 2 epochs' iterations and then decreases by a ratio of 0.1 every 10 epochs. ADAM optimizer is used in the training process.

C. Experimental Results and Analysis

1) *Ablation Study on Label Assignment Strategies*: Experiments on Oxford Radar RobotCar dataset are performed to evaluate the effectiveness of the proposed strategies. Since the annotation has only one type of labeled car class, the AP is used only for cars. The evaluation metrics of AP at

IoU 0.5, 0.65, and 0.8 are chosen to demonstrate changes in performance.

Table II presents the experiment results of different label assignment strategies and interactive transformer fusion architectures of our proposed RaLiBEV. It is noted that the performance of the **Gaussian Area-based Multi-Positive Sample Assignment** strategy serves as a solid baseline thanks to the use of YOLOv4 backbone and neck in our RaLiBEV framework, which is similar to the core design of PillarNeXt [69]. The AP of IoU of 0.5 and 0.65 is 95.4% and 94.2%, both improve 2.2%, but show a 5.8% drop of AP at IoU of 0.8, falling down to 75.7% compared to the ST-MVDNet++ [52]. The AP performance of the state-of-the-art ST-MVDNet++ [52] at IoU 0.5, 0.65, and 0.8 are 93.2%, 92.0%, and 81.5%, respectively.

The second type of label assignment strategy is **DIPS Assignment**. The improvement presented by this strategy is not significant at the low precision AP result at IoU of 0.5 and 0.65, approximately around 0.7% - 0.9%. Still, better performance at high precision AP at IoU of 0.8 results about 6% compares to the first strategy above. The result of the third strategy illustrates the effectiveness of choosing a more appropriate positive-sample strategy. Compared to the previous strategy, the performance of **GAHPS** shows another performance improvement of about 5% in high precision, which reaches 89.5% AP at IoU of 0.8. Following this approach, in **GAHIPS**, the performance at an IoU of 0.5 remains almost the same as the previous strategy, while the most notable change is in AP at an IoU of 0.8. The performance breaks through to 92.0%, which is a significant improvement of 10.5% compared to the 81.5% of the state-of-the-art ST-MVDNet++.

The above single positive label assignment strategies are based on encouraging the best box regression predicted key point to approach the classification predicted key point. These

TABLE II
ABLATION STUDY OF RALiBEV ANCHOR BOX FREE OBJECT DETECTOR.

Methods	AP@IoU=0.5	AP@IoU=0.65	AP@IoU=0.8
Proposed RaLiBEV with Different Label Assignments and Plain BEV Fusion (Ours)			
Gaussian Area-based Multi-Positives Sample Assignment	95.4	94.2	75.7
Direct Index-based Positive Sample assignment (DIPS)	96.3	94.9	84.5
Gaussian Area-based Heatmap cost Positive Sample assignment (GAHPS)	96.7	95.4	89.5
Gaussian Area-based Heatmap and IoU cost Positive Sample assignment (GAHIPS)	96.8	96.7	92.0
Gaussian Area-based Consistent Heatmap and IoU cost Positive Sample assignment (GACHIPS)	97.4	96.7	93.9
Proposed RaLiBEV with Interactive Transformer-based BEV Fusion (Ours)			
Direct Transformer for BEV Fusion	97.8	97.5	92.3
Dense Query Map-based Interactive Transformer for BEV Fusion (DQMITBF)	98.8	97.7	94.8

TABLE III

COMPARISON OF LiDAR ONLY APPROACHES AND RALiBEV WHICH EMPLOYS FUSION OF RADAR AND LiDAR. THE NUMBERS IN BOLD ARE THE BEST OF ALL METHODS.

Method	Train Test IoU	Modality	Clear+Foggy						Clear-only					
			Clear			Foggy			Clear			Foggy		
			0.5	0.65	0.8	0.5	0.65	0.8	0.5	0.65	0.8	0.5	0.65	0.8
PointPillars		L	85.8	83.0	58.3	72.8	70.3	48.6	85.8	82.9	60.6	71.3	68.3	47.8
RaLiBEV LiDAR-Only		L	96.3	93.8	78.3	92.2	88.3	74.4	97.7	96.4	87.5	68.2	62.7	40.2
RaLiBEV with GACHIPS (Ours)		L+R	97.8	97.7	93.9	97.8	96.7	93.7	97.4	96.7	93.9	84.6	82.4	73.8
RaLiBEV with DQMITBF (Ours)		L+R	98.8	97.7	95.1	97.9	97.8	94.1	98.8	97.7	94.8	83.3	80.9	70.6

TABLE IV

COMPARISON OF AP OF ORIENTED BOUNDING BOXES IN BIRD’S EYE VIEW BETWEEN OUR PROPOSED RALiBEV AND OTHER STATE-OF-THE-ART RADAR AND LiDAR FUSION-BASED METHODS. THE NUMBERS IN BOLD ARE THE BEST OF ALL METHODS.

Method	Train Test IoU	Modality	Clear+Foggy						Clear-only					
			Clear			Foggy			Clear			Foggy		
			0.5	0.65	0.8	0.5	0.65	0.8	0.5	0.65	0.8	0.5	0.65	0.8
DEF (CVPR2020) [48]		L+R	86.6	78.2	46.2	81.4	72.5	41.1	85.9	78.1	44.2	71.8	63.7	32.4
MVDNet (CVPR2021) [24]		L+R	90.9	88.8	74.6	87.4	84.6	68.9	87.2	86.1	72.6	78.0	75.9	61.6
Bi-LRFusion (CVPR2023) [53]		L+R	92.2	N/A	74.4	N/A								
ST-MVDNet (CVPR2022) [25]		L+R	94.7	93.5	80.7	91.8	88.3	73.6	91.4	89.9	78.4	81.2	80.8	64.9
ST-MVDNet++ (ICASSP 2023) [52]		L+R	96.0	94.7	82.0	93.4	90.0	75.1	93.2	92.0	81.5	83.7	83.2	67.5
RaLiBEV with GACHIPS (Ours)		L+R	97.8	97.7	93.9	97.8	96.7	93.7	97.4	96.7	93.9	84.6	82.4	73.8
RaLiBEV with DQMITBF (Ours)		L+R	98.8	97.7	95.1	97.9	97.8	94.1	98.8	97.7	94.8	83.3	80.9	70.6

types of ideas have shown great validity. However, in the following strategy, a strong binding strategy has been experimented with. **GACHIPS** inherits the previous strategy, using heatmap and IoU as cost, while calculating foreground-background classification loss and box loss after finding the best-matched anchor point. The final result shows further improvement at AP of IoU 0.5 and 0.8, which increased to 97.4% and 93.9%, respectively.

Experiments indicate that a **multi-positive sample** strategy can reduce a model’s high-precision performance. The reason is that calculating multiple losses for the same ground truth object introduces competition between samples. Specifically, the current loss design includes Δx and Δy , which are related to the sample’s position. These supervision values vary by location, with points further from the center having larger values. This means that different positive samples for the same ground truth object have inconsistent regression endpoints, preventing the model from converging well near the extremes. In traditional image detection, multi-positive sample assign-

ment strategies are popular for improving detection rates under overlap conditions. However, this approach is not suitable for BEV perception in autonomous driving, as targets do not overlap each other in BEV.

However, the assumption of a single positive sample point effectively avoids this competition, creating a singular convergence point for the model. Yet, inconsistencies between foreground-background classification and bounding box regression with a single positive sample point can limit the model’s ultimate performance. Specifically, when employing the **DIPS** strategy, the model uses a fixed target center point to calculate box regression loss, but the optimal point for foreground-background classification during inference may not be at the target center, leading to a loss in model accuracy. This design has a typical inconsistency issue between classification and regression. Therefore, the **GAHPS** strategy aims to find a way to ensure that the best foreground point during inference is also the one that has undergone the most box regression training by the end of training. Hence, during each training

session, the peak points of the forward inference heatmap are selected as the anchor points for box regression. This strategy indeed brought an improvement in model performance. Compared to DIPS, its high-precision IoU 0.8 performance increased by 5%.

After observing the aforementioned performance improvements, we hypothesized that a better cost design would further enhance model accuracy. Thus, we replaced the original heatmap with a heatmap plus IoU, hoping to further reduce inconsistencies. Experiments show that this understanding is correct, and the model indeed achieved further improvements in high-precision performance. Compared to GAHPS, **GAHIPS** improved by 2.5% at IoU 0.8. Furthermore, we attempted to have the selected positive sample control both the foreground-background classification and the bounding box regression loss, proposing **GACHIPS**. This modification means that we have theoretically maximized the consistency between above two calculations. Specifically, during the training phase, the model uses the best anchor point obtained from inference for loss calculation. Then, during inference, it decodes the best detection box through this optimal anchor point. This design achieves unity between foreground-background classification and bounding box regression, ensuring consistency between the training and inference stages. Experiments show that this approach achieved the best high-precision performance, reaching 93.9% at IoU 0.8.

2) *Ablation Study on Interactive Transformer-based BEV Fusion Approaches*: To illustrate the effectiveness of interactive transformer-based BEV fusion approaches, both the direct transformer and interactive transformer are applied in fusion module with DIPS label assignment, respectively. Table II presents the results of transformers as well. In the **Direct Transformer for BEV Fusion**, the performance reached the same level as GACHIPS with only slightly lower performance, around 1.6% in high precision IoU of 0.8. While the **DQMITBF** exhibits stronger performance, all three indicators exceed GACHIPS in an all-around way. This brings the AP result of IoU 0.5, 0.65, and 0.8 to 98.8%, 97.7%, and 94.8%, respectively.

To demonstrate the effectiveness of DQMITBF in a more comprehensible manner, the feature maps of two selected two frames in the interactive transformer fusion module are visualized as depicted in Fig. 5. In Fig. 5, The top two rows are corresponding to Frame 2799 and the bottom two rows are corresponding to Frame 3299, which are selected randomly. Each frame includes selections from clear and foggy weather conditions for analysis. For each column, the feature maps \mathbf{X}_Q , \mathbf{X}_R , \mathbf{X}_L , $\mathbf{X}_Q\mathbf{X}_R^T$, and $\mathbf{X}_Q\mathbf{X}_L^T$ are illustrated for visual comprehension. Furthermore, all feature maps are normalized to the range [0, 1] for a consistent representation.

Utilizing a unified BEV query \mathbf{X}_Q , the input radar feature map \mathbf{X}_R and LiDAR feature map \mathbf{X}_L are weighted to $\mathbf{X}_Q\mathbf{X}_R^T$ and $\mathbf{X}_Q\mathbf{X}_L^T$ respectively, subsequently producing a fused feature for additional processing. It can be observed that \mathbf{X}_Q manages radar and LiDAR features differently under varying weather conditions. In clear weather, $\mathbf{X}_Q\mathbf{X}_L^T$ is noticeably larger in numerical value than $\mathbf{X}_Q\mathbf{X}_R^T$. However, in foggy conditions, the input \mathbf{X}_L is significantly impacted by noise,

resulting in $\mathbf{X}_Q\mathbf{X}_R^T$ being larger than $\mathbf{X}_Q\mathbf{X}_L^T$. From these observations, we can draw the following conclusions:

- The approach utilizes an interactive transformer to aggregate data from LiDAR and radar branches in a unified manner;
- The BEV query in the interactive transformer can focus on more information-rich signals under different weather conditions.

Additionally, as depicted in Fig. 5, the input \mathbf{X}_L and \mathbf{X}_R appear visually similar to the raw source data, and \mathbf{X}_Q does not seem to focus on a specific area determined by the presence of an object. This is because the interactive transformer fusion module operates in the encoder process of the entire model at an early stage, where the data feature resides in a raw energy distribution space rather than a box location feature space.

The result of the experiment shows that a reasonable fusion logic would significantly enhance the performance of the proposed RaLiBEV. While direct transformer fusion among feature maps can enhance performance, the implementation of interactive transformer-based concepts can yield superior results. This is largely due to the innovative querying fusion method, which introduces symmetry and unifying properties into the model.

To also highlight the benefits of multi-modality fusion, Table III presents a comparison of performance metrics between the LiDAR-only approach and the fusion of radar and LiDAR. It is evident from the comparison that neither RaLiBEV with LiDAR only nor PointPillars can match the performance levels achieved by the fusion of radar and LiDAR. This performance enhancement is particularly noticeable in foggy testing scenarios. When the model is trained on a “Clear+Foggy” dataset, RaLiBEV, in the radar and LiDAR fusion modality (denoted as “R+L”), exhibits exceptionally high performance, especially under the stringent requirements of a 0.8 IoU in “Foggy” test scenarios.

3) *Performance Comparison with State-of-the-Art Methods on Different Weather Conditions*: Following MVDNet [24], model performance in different weather is tested in this paper as described in Table IV. The simulated foggy LiDAR data is generated by the code provided by MVDNet. This experiment is set as training using “Clear-only” and “Clear+Foggy” LiDAR and radar data, then testing under both “Clear” and “Foggy” data. Two peak performance models are chosen to prove their capability under this condition. One is RaLiBEV with GACHIPS, the other is RaLiBEV with DQMITBF. The performance of GACHIPS training under “Clear-only” data and testing under the “Foggy” scenario is better than DQMITBF’s. The performance of the horizontal comparison model after data enhancement is about 10%. GACHIPS increases from 84.6%, 82.4%, and 73.8% to 97.8%, 96.7%, and 93.7% under the “Foggy” test. This result exceeds the ST-MVDNet [25] over 20% at “Clear+Foggy” training and “Foggy” test scenario. Compared to the newest work Bi-LRFusion [53], RaLiBEV outperforms a large margin of 20.7% in IoU 0.8 requirement. Meanwhile, according to the results of the state-of-art work ST-MVDNet++ [52], RaLiBEV has made progress of 4.4%, 7.8% and 19.0% in IoU 0.5, 0.65 and 0.8 under “Clear+Foggy” training, “Foggy” test.

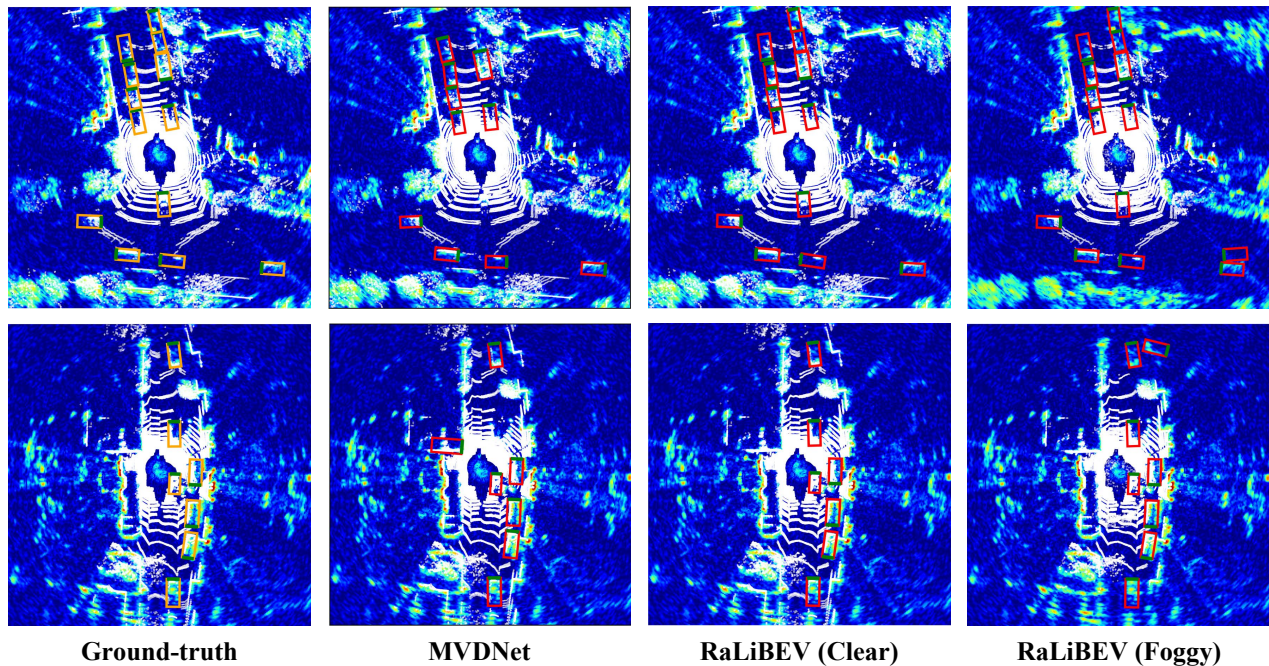


Fig. 6. Visualization of detection results of MVDNet and RaLiBEV.

This result represents that RaLiBEV is able to perform better accuracy in adverse weather such as fog. The fusion logic and label assignment strategy help the detector achieves higher precision.

Fig. 6 shows the ground-truth, the prediction from MVDNet in clear weather, the prediction from RaLiBEV in clear weather and foggy weather at the 3332th and 4103th frame of test dataset. The ground-truth bounding boxes are decorated with yellow color, and the predicted boxes by each model are shown with red color. All boxes use green lines to indicate the heading of the object. It is easy to find out that the prediction of MVDNet have 3 miss detection and 4 predicted boxes with reversed heading direction in the top row figure, and 1 false alarm and 2 reversed predicted boxes in the bottom row figure, though the weather is clear. In contrast, The RaLiBEV shows perfect detection results in clear weather, and only gives one false detection and no reversed heading prediction in both time frame under foggy weather.

V. CONCLUSION

In this paper, we introduce RaLiBEV, an innovative method for fusing LiDAR and radar data. According to the experiment results, this method effectively showcases the significant role that radar can play in fusing autonomous driving perception technology, especially in adverse weather. To enhance the performance of the model, especially for high-precision detection, novel label assignment and transformer-based fusion strategies are proposed. Specifically, the GACHIPS strategy is proposed to dynamically adjust the classification and regression positive sample position, to solve the inconsistency problem in the loss procedure. Meanwhile, the DQMITBF is proposed to aggregate weighted features from different sensor data. Thanks to the interaction of the dense learnable query with radar and

LiDAR in the symmetrical manner, RaLiBEV can switch the focus on different sensor modalities adaptively, according to change of the perception environment and weather conditions. It's also noteworthy that by incorporating the GACHIPS label assignment into a simple fusion architecture, the model can attain performance on par with the more intricate transformer fusion. The experiments with ORR dataset show that RaLiBEV exceeds all existing state-of-the-art approaches by a large margin.

REFERENCES

- [1] X. Zhu et al., "Interaction-aware cut-in trajectory prediction and risk assessment in mixed traffic," *IEEE/CAA Journal of Automatica Sinica*, vol. 9, no. 10, pp. 1752-1762, Oct. 2022.
- [2] L. Chen, X. Hu, W. Tian, H. Wang, D. Cao and F. -Y. Wang, "Parallel planning: A new motion planning framework for autonomous driving," *IEEE/CAA Journal of Automatica Sinica*, vol. 6, no. 1, pp. 236-246, Jan. 2019.
- [3] D. Barnes, M. Gadd, P. Murcutt, P. Newman, and I. Posner, "The oxford radar robotcar dataset: A radar extension to the oxford robotcar dataset," in *Proceedings of IEEE International Conference on Robotics and Automation (ICRA)*, 2020, pp. 6433-6438.
- [4] A. Li, S. Chen, L. Sun, N. Zheng, M. Tomizuka, and W. Zhan, "SceGene: Bio-inspired traffic scenario generation for autonomous driving testing," *IEEE Transactions on Intelligent Transportation Systems*, vol. 23, no. 9, pp. 14859-14874, Sept. 2022.
- [5] A. Chalvatzaras, I. Pratikakis, and A. A. Amanatiadis, "A survey on map-based localization techniques for autonomous vehicles," *IEEE Transactions on Intelligent Vehicles* vol. 8, no. 2, pp. 1574-1596, Feb. 2023.
- [6] D. J. Fremont, E. Kim, Y. V. Pant, S. A. Seshia, A. Acharya, X. Brusio, P. Wells, S. Lemke, Q. Lu, and S. Mehta. "Formal scenario-based testing of autonomous vehicles: From simulation to the real world," in *Proceedings of the IEEE International Conference on Intelligent Transportation Systems (ITSC)*, 2020, pp. 1-8.

- [7] S. Chen, B. Liu, C. Feng, C. Vallespi-Gonzalez, and C. Wellington, "3D point cloud processing and learning for autonomous driving: Impacting map creation, localization, and perception," *IEEE Signal Processing Magazine*, vol. 38, no. 1, pp. 68-86, Jan. 2021.
- [8] T. Yin, X. Zhou, and P. Krahenbuhl, "Center-based 3D object detection and tracking," in *Proceedings of the IEEE/CVF Conference on Computer Vision and Pattern Recognition (CVPR)*, 2021, pp. 11784-11793.
- [9] A. Lang, S. Vora, H. Caesar, L. Zhou, J. Yang, and O. Beijbom, "Pointpillars: Fast encoders for object detection from point clouds," in *Proceedings of the IEEE/CVF Conference on Computer Vision and Pattern Recognition (CVPR)*, 2019, pp. 12697-12705.
- [10] J. Liu, L. Bai, Y. Xia, T. Huang, B. Zhu, and Q.-L. Han, "GNN-PMB: A simple but effective online 3D multi-object tracker without bells and whistles," *IEEE Transactions on Intelligent Vehicles*, vol. 8, no. 2, pp. 1176-1189, Feb. 2023.
- [11] Z. Zhang, J. Liu, Y. Xia, T. Huang, Q.-L. Han, and H. Liu, "LEGO: Learning and graph-optimized modular tracker for online multi-object tracking with point clouds," 2023, *arXiv:2308.09908*.
- [12] S. Liang, Z. Cao, C. Wang, and J. Yu, "Hierarchical estimation-based lidar odometry with scan-to-map matching and fixed-lag smoothing," *IEEE Transactions on Intelligent Vehicles*, vol. 8, no. 2, pp. 1607-1623, Feb. 2023.
- [13] H. Guo, J. Zhu, and Y. Chen, "E-LOAM: LiDAR odometry and mapping with expanded local structural information," *IEEE Transactions on Intelligent Vehicles*, vol. 8, no. 2, pp. 1911-1921, Feb. 2023.
- [14] L. Wang, X. Zhang, Z. Song, J. Bi, G. Zhang, H. Wei, L. Tang, L. Yang, J. Li, C. Jia, and L. Zhao, "Multi-Modal 3D object detection in autonomous driving: A survey and taxonomy," *IEEE Transactions on Intelligent Vehicles*, vol. 8, no. 7, pp. 3781-3798, Jul. 2023.
- [15] S. Richter, F. Bieder, S. Wirges, and C. Stiller, "A dual evidential top-view representation to model the semantic environment of automated vehicles," *IEEE Transactions on Intelligent Vehicles*, doi: 10.1109/TIV.2023.3284400.
- [16] S. Hasirliglu and A. Riener, "A general approach for simulating rain effects on sensor data in real and virtual environments," *IEEE Transactions on Intelligent Vehicles*, vol. 5, no. 3, pp. 426-438, Sept. 2020.
- [17] M. Dreißig, D. Scheuble, F. Piewak, and J. Boedecker, "Survey on LiDAR perception in adverse weather conditions," in *Proceedings of the IEEE Intelligent Vehicles Symposium (IV)*, 2023, pp. 1-8.
- [18] S. Sun, A. P. Petropulu, and H. V. Poor, "MIMO radar for advanced driver-assistance systems and autonomous driving: Advantages and challenges," *IEEE Signal Processing Magazine*, vol. 37, no. 4, pp. 98-117, June 2020.
- [19] T. Huang, J. Liu, X. Zhou, D. C. Nguyen, M. R. Azghadi, Y. Xia, Q.-L. Han, and S. Sun, "V2X cooperative perception for autonomous driving: Recent advances and challenges," 2023, *arXiv:2310.03525*.
- [20] J. Liu, Q. Zhao, W. Xiong, T. Huang, Q.-L. Han, and B. Zhu, "SMURF: Spatial multi-representation fusion for 3D object detection with 4D imaging radar," *IEEE Transactions on Intelligent Vehicles*, Oct. 2023, doi: 10.1109/TIV.2023.3322729.
- [21] L. Zheng, S. Li, B. Tan, L. Yang, S. Chen, L. Huang, J. Bai, X. Zhu, and Z. Ma, "RCFusion: Fusing 4D radar and camera with bird's-eye view features for 3D object detection," *IEEE Transactions on Instrumentation and Measurement*, vol. 72, pp. 1-14, May 2023.
- [22] W. Xiong, J. Liu, T. Huang, Q.-L. Han, Y. Xia, and B. Zhu, "LXL: LiDAR excluded lean 3D object detection with 4D imaging radar and camera fusion," *IEEE Transactions on Intelligent Vehicles*, Oct. 2023, doi: 10.1109/TIV.2023.3321240.
- [23] J. Liu, G. Ding, Y. Xia, J. Sun, T. Huang, L. Xie, and B. Zhu, "Which framework is suitable for online 3D multi-object tracking for autonomous driving with automotive 4D imaging radar?" 2023, *arXiv:2309.06036*.
- [24] K. Qian, S. Zhu, X. Zhang, and L. E. Li, "Robust multimodal vehicle detection in foggy weather using complementary lidar and radar signals," in *Proceedings of the IEEE/CVF Conference on Computer Vision and Pattern Recognition (CVPR)*, 2021, pp. 444-453.
- [25] Y. Li, J. Park, M. O' Toole, and K. Kitani, "Modality-agnostic learning for radar-lidar fusion in vehicle detection," in *Proceedings of the IEEE/CVF Conference on Computer Vision and Pattern Recognition (CVPR)*, 2022, pp. 918-927.
- [26] C. Qi, H. Su, K. Mo, and L. J. Guibas, "Pointnet: Deep learning on point sets for 3d classification and segmentation," in *Proceedings of IEEE Conference Computer Vision Pattern Recognition (CVPR)*, 2017, pp. 652-660.
- [27] C. Qi, L. Yi, H. Su, and L. J. Guibas, "Pointnet++: Deep hierarchical feature learning on point sets in a metric space," in *Proceedings of the Conference on Advances in Neural Information Processing Systems (NeurIPS)*, 2017, pp. 5099-5108.
- [28] D. Maturana and S. Scherer, "Voxnet: A 3d convolutional neural network for real-time object recognition," in *Proceedings of IEEE/RSJ International Conference on Intelligent Robots and Systems (IROS)*, 2015, pp. 922-928.
- [29] C. He, R. Li, S. Li, and L. Zhang, "Voxel set transformer: A set-to-set approach to 3d object detection from point clouds," in *Proceedings of the IEEE/CVF Conference on Computer Vision and Pattern Recognition (CVPR)*, 2022, pp. 8417-8427.
- [30] W. Shi and R. Rajkumar, "Point-GNN: Graph neural network for 3d object detection in a point cloud," in *Proceedings of the IEEE/CVF Conference on Computer Vision and Pattern Recognition (CVPR)*, 2020, pp. 1711-1719.
- [31] J. S. Hu, T. Kuai, and S. L. Waslander, "Point density-aware voxels for lidar 3d object detection," in *Proceedings of the IEEE/CVF Conference on Computer Vision and Pattern Recognition (CVPR)*, 2022, pp. 8469-8478.
- [32] A. Laddha, S. Gautam, S. Palombo, S. Pandey, and C. Vallespi-Gonzalez, "MVFuseNet: Improving end-to-end object detection and motion forecasting through multi-view fusion of lidar data," in *Proceedings of the IEEE/CVF Conference on Computer Vision and Pattern Recognition (CVPR)*, 2021, pp. 2865-2874.
- [33] M. Kronauge and H. Rohling, "Fast two-dimensional CFAR procedure," *IEEE Transactions on Aerospace and Electronic Systems*, vol. 49, no. 3, pp. 1817-1823, July 2013.
- [34] S. Lim, S. Lee, and S. -C. Kim, "Clustering of detected targets using DBSCAN in automotive radar systems," in *Proceedings of the 19th International Radar Symposium (IRS)*, 2018, pp. 1-7.
- [35] J. Liu, W. Xiong, L. Bai, Y. Xia, T. Huang, W. Ouyang, and B. Zhu, "Deep instance segmentation with automotive radar detection points," *IEEE Transactions on Intelligent Vehicles*, vol. 8, no. 1, pp. 84-94, Jan. 2023.
- [36] W. Xiong, J. Liu, Y. Xia, T. Huang, B. Zhu, and W. Xiang, "Contrastive learning for automotive mmWave radar detection points based instance segmentation," in *Proceedings of the IEEE International Conference on Intelligent Transportation Systems (ITSC)*, 2022, pp. 1255-1261.
- [37] A. Danzer, T. Griebel, M. Bach, and K. Dietmayer, "2D car detection in radar data with PointNets," in *Proceedings of the IEEE International Conference on Intelligent Transportation Systems (ITSC)*, 2019, pp. 61-66.
- [38] M. M. Dreher, E. Erçelik, T. Bänziger, and A. Knol, "Radar-based 2D car detection using deep neural networks," in *Proceedings of the IEEE International Conference on Intelligent Transportation Systems (ITSC)*, 2020, pp. 1-8.
- [39] P. Svenningsson, F. Fioranelli, and A. Yarovoy, "Radar-PointGNN: Graph based object recognition for unstructured radar point-cloud data," in *Proceedings of the IEEE Radar Conference (RadarConf)*, 2021, pp. 1-6.

- [40] M. Meyer, G. Kuschik, and S. Tomforde, "Graph convolutional networks for 3D object detection on radar data," in *Proceedings of IEEE/CVF International Conference on Computer Vision Workshop (ICCVW)*, 2021, pp. 3060-3069.
- [41] K. Patel, K. Rambach, T. Visentin, D. Rusev, M. Pfeiffer, and B. Yang, "Deep learning-based object classification on automotive radar spectra," in *Proceedings of the IEEE Radar Conference (RadarConf)*, 2019, pp. 1-6.
- [42] A. Cozma, L. Morgan, M. Stolz, D. Stoeckel, and K. Rambach, "DeepHybrid: Deep learning on automotive radar spectra and reflections for object classification," in *Proceedings of IEEE Intelligent Transportation Systems Conference (ITSC)*, 2021, pp. 2682-2687.
- [43] B. Major, D. Fontijne, A. Ansari, R. T. Sukhavasi, R. Gowaikar, M. Hamilton, S. Lee, S. Grzechnik, and S. Subramanian, "Vehicle detection with automotive radar using deep learning on range-azimuth-doppler tensors," in *Proceedings of IEEE/CVF International Conference on Computer Vision Workshop (ICCVW)*, 2019, pp. 924-932.
- [44] C. Decourt, R. Vanrullen, D. Salle, and T. Oberlin, "DAROD: A deep automotive radar object detector on range-doppler maps," in *Proceedings of IEEE Intelligent Vehicles Symposium (IV)*, 2022, pp. 112-118.
- [45] C. Decourt, R. Vanrullen, D. Salle, and T. Oberlin, "A recurrent CNN for online object detection on raw radar frames," 2022, *arXiv:2212.11172*.
- [46] P. Li, P. Wang, K. Berntorp, and H. Liu, "Exploiting temporal relations on radar perception for autonomous driving," in *Proceedings of IEEE/CVF Conference on Computer Vision and Pattern Recognition (CVPR)*, 2022, pp. 17071-17080.
- [47] T.-Y. Huang, M.-C. Lee, C.-H. Yang, and T.-S. Lee, "YOLO-ORE: A deep learning-aided object recognition approach for radar systems," *IEEE Transactions on Vehicular Technology*, vol. 72, no. 5, pp. 5715-5731, May 2023.
- [48] M. Bijelic, T. Gruber, F. Mannan, F. Kraus, W. Ritter, K. Dietmayer, and F. Heide, "Seeing through fog without seeing fog: Deep multimodal sensor fusion in unseen adverse weather," in *Proceedings of the IEEE/CVF Conference on Computer Vision and Pattern Recognition (CVPR)*, 2020, pp. 11682-11692.
- [49] L. Wang, X. Zhang, B. Xv, J. Zhang, R. Fu, X. Wang, L. Zhu, H. Ren, P. Lu, J. Li, and H. Liu, "InterFusion: Interaction-based 4D radar and LiDAR fusion for 3D object detection," in *Proceedings of the IEEE/RSJ International Conference on Intelligent Robots and Systems (IROS)*, 2022, pp. 12247-12253.
- [50] L. Wang, X. Zhang, J. Li, B. Xv, R. Fu, H. Chen, L. Yang, D. Jin, and L. Zhao, "Multi-modal and multi-scale fusion 3D object detection of 4D radar and LiDAR for autonomous driving," *IEEE Transactions on Vehicular Technology*, vol. 72, no. 5, pp. 5628-5641, May 2023.
- [51] A. Vaswani, N. Shazeer, N. Parmar, J. Uszkoreit, L. Jones, A. N. Gomez, Ł. Kaiser, and I. Polosukhin, "Attention is all you need," in *Proceedings of the Conference on Advances in Neural Information Processing Systems (NeurIPS)*, 2017, pp. 5998-6008.
- [52] Y. Li, M. O' Toole, and K. Kitani, "ST-MVDNet++: Improve vehicle detection with lidar-radar geometrical augmentation via self-training," in *Proceedings of the IEEE International Conference on Acoustics, Speech and Signal Processing (ICASSP)*, 2023, pp. 1-5.
- [53] Y. Wang, J. Deng, Y. Li, J. Hu, C. Liu, Y. Zhang, J. Ji, W. Ouyang, and Y. Zhang, "Bi-LRFusion: Bi-directional LiDAR-radar fusion for 3D dynamic object detection," in *Proceedings of the IEEE/CVF Conference on Computer Vision and Pattern Recognition (CVPR)*, 2023, pp. 13394-13403.
- [54] S. Li, C. H. He, H. Chen, R. H. Li, and L. Zhang, "A dual weighting label assignment scheme for object detection," in *Proceedings of the IEEE/CVF Conference on Computer Vision and Pattern Recognition (CVPR)*, 2022, pp. 9387-9396.
- [55] R. Girshick, "Fast R-CNN," in *Proceedings of the IEEE International Conference on Computer Vision (ICCV)*, 2015, pp. 1440-1448.
- [56] J. Redmon, S. Divvala, R. Girshick, and A. Farhadi, "You only look once: Unified, real-time object detection," in *Proceedings of the IEEE/CVF Conference on Computer Vision and Pattern Recognition (CVPR)*, 2016, pp. 779-788.
- [57] Z. Tian, C. Shen, H. Chen, and T. He, "FCOS: Fully convolutional one-stage object detection," in *Proceedings of the International Conference on Computer Vision (ICCV)*, 2019, pp. 9626-9635.
- [58] K. Duan, S. Bai, L. Xie, H. Qi, Q. Huang, and Q. Tian, "CenterNet: Keypoint triplets for object detection," in *Proceedings of the International Conference on Computer Vision (ICCV)*, 2019, pp. 6568-6577.
- [59] H. Law and J. Deng, "CornerNet: Detecting objects as paired keypoints," in *Proceedings of the European Conference on Computer Vision (ECCV)*, 2020, pp. 642-656.
- [60] X. Zhang, F. Wan, C. Liu, R. Ji, and Q. Ye, "FreeAnchor: Learning to match anchors for visual object detection," *Advances in Neural Information Processing Systems*, 2019, pp. 147-155.
- [61] S. Zhang, C. Chi, Y. Yao, Z. Lei, and S. Li, "Bridging the gap between anchor-based and anchor-free detection via adaptive training sample selection," in *Proceedings of the IEEE/CVF Conference on Computer Vision and Pattern Recognition (CVPR)*, 2020, pp. 9759-9768.
- [62] B. Zhu, J. Wang, Z. Jiang, F. Zong, S. Liu, Z. Li, and J. Sun, "AutoAssign: Differentiable label assignment for dense object detection," 2020, *arXiv:2007.03496*.
- [63] C. H. Nguyen, T. C. Nguyen, T. N. Tang, and N. L. Phan, "Improving object detection by label assignment distillation," in *Proceedings of the IEEE/CVF Winter Conference on Applications of Computer Vision (WACV)*, 2022, pp. 1005-1014.
- [64] Z. Ge, S. Liu, Z. Li, O. Yoshie, and J. Sun, "OTA: Optimal transport assignment for object detection," in *Proceedings of the IEEE/CVF Conference on Computer Vision and Pattern Recognition (CVPR)*, 2021, pp. 303-312.
- [65] A. Bochkovskiy, C. Wang, and H. Liao, "YOLOv4: Optimal speed and accuracy of object detection," 2020, *arXiv:2004.10934*.
- [66] T.-Y. Lin, P. Goyal, R. Girshick, K. He, and P. Dollár, "Focal loss for dense object detection," in *Proceedings of the IEEE International Conference on Computer Vision (ICCV)*, 2017, pp. 2980-2988.
- [67] D. Erhan, C. Szegedy, A. Toshev, and D. Anguelov, "Scalable object detection using deep neural networks," in *Proceedings of the IEEE/CVF Conference on Computer Vision and Pattern Recognition (CVPR)*, 2014, pp. 2147-2154.
- [68] N. Carion, F. Massa, G. Synnaeve, N. Usunier, A. Kirillov, and S. Zagoruyko, "End-to-end object detection with transformers," in *Proceedings of the European Conference on Computer Vision (ECCV)*, 2020, pp. 213-229.
- [69] J. Li, C. Luo, and X. Yang, "PillarNeXt: Rethinking network designs for 3D object detection in LiDAR point clouds," in *Proceedings of the IEEE/CVF Conference on Computer Vision and Pattern Recognition (CVPR)*, 2023, pp. 17567-17576.